# Supporting information for the paper:

## Effect of Carbon-skeleton Isomerism on Dielectric Property and Proton Conduction of Organic Cocrystal Compounds Assembled from 1,2,4,5-Benzenetetracarboxylic Acid and Piperazine Derivatives

Xiaoqiang Liang, [*] [a] Yixiang Chen, [b] Li Wang, [a] Feng Zhang,[*] [c] Zenglu Fan,[*] [b] Tingting Cao,[a] Yaya Cao,[a] Huifang Zhu,[a] Xinyue He,[a] Bolin Deng,[a] Yazhi You,[a] Yu Dong [a] and Yamei Zhao [a]

[a] *College of Environmental and Chemical Engineering, Xi'an Polytechnic University, Xi'an 710048, PR China*

[b] *College of Textile Science and Engineering, Xi'an Polytechnic University, Xi'an 710048, PR China*

[c] *Key Laboratory of Photochemical Biomaterials and Energy Storage Materials, Heilongjiang Province and College of Chemistry and Chemical Engineering, Harbin Normal University, Harbin 150025, PR China*

# Table of Contents

Crystal data and Structures ·····S2–S5

Infrared Absorption Spectra ·····S6

Powder X-ray Diffraction Patterns·····S7

Thermogravimetric Analysis Curves ·····S8

Dielectric Properties ·····S9–S13

Melting Point Measurements ·····S14–S15

Powder X-ray Diffraction Patterns after Dielectric Measurements ·····S16

Raman Spectroscopy ·····S17–S18

Proton-conducting Properties ·····S19–S24

Powder X-ray Diffraction Patterns after Proton-conducting Measurements ·····S25

**Table S1.** Hydrogen-bonding geometry parameters (Å, °) for OCC **1** and OCC **2**

| D−H···A | d(D−H) | d(H···A) | d(D···A) | ∠(DHA) |
|---|---|---|---|---|
| | | OCC 1 | | |
| O(2)−H(2)···O(6a) | 0.85 | 1.80 | 2.6368(15) | 167 |
| O(4)−H(4A)···O(3b) | 0.85 | 2.58 | 3.3660(17) | 154 |
| O(7)−H(7)···O(3c) | 0.85 | 1.78 | 2.6279(15) | 172 |
| O(7)−H(7)···O(4c) | 0.85 | 2.63 | 3.1517(15) | 121 |
| O(1W)−H(1WA)···O(5) | 0.903(17) | 2.19(2) | 3.014(2) | 151 |
| N(12)−H(2A)···O(1Wd) | 0.89 | 1.89 | 2.778(13) | 172 |
| N(12)−H(2B)···O(8e) | 0.89 | 1.96 | 2.754(13) | 148 |
| N(14)−H(14C)···O(1Wc) | 0.97 | 2.29 | 3.064(4) | 136 |
| N(14)−H(14D)···O(8f) | 0.97 | 2.09 | 2.753(5) | 124 |
| | | OCC 2 | | |
| O(1W)−H(1WD)···O(14a) | 0.85 | 2.49 | 3.0618(18) | 126 |
| N(1)−H(1A)···O(11) | 0.90 | 1.86 | 2.616(2) | 141 |
| N(1)−H(1B)···O(1W) | 0.90 | 1.90 | 2.790(2) | 172 |
| O(1)−H(1C)···O(5a) | 0.85 | 2.27 | 2.5834(17) | 102 |
| O(1W)−H(1WC)···O(1b) | 0.85 | 2.56 | 3.1865(17) | 131 |
| O(1W)−H(1WC)···O(6a) | 0.85 | 2.33 | 2.9118(18) | 126 |
| N(2)−H(2A)···O(8a) | 0.89 | 2.01 | 2.738(2) | 138 |
| O(3)−H(3A)···O(7b) | 0.85 | 2.55 | 3.2469(18) | 140 |
| O(7)−H(7A)···O(4c) | 0.85 | 1.81 | 2.6145(19) | 158 |
| O(12)−H(12C)···O(15b) | 0.85 | 1.92 | 2.5268(19) | 127 |
| O(13)−H(13A)···O(10d) | 0.85 | 1.94 | 2.7239(18) | 153 |
| O(16)−H(16A)···O(12c) | 0.85 | 2.46 | 3.1702(19) | 142 |

Symmetry codes : a)+*x*,+*y*,1+*z*; b)1−*x*, −*y*, −*z*; c) −1+*x*,1+*y*,+*z*; d)1−*x*,1−*y*, −1−*z*; e) −*x*, 2−*y*, −*z*; f) +*x*,+*y*,−1+*z* for OCC **1**; a) −1+*x*, *y*, *z*; b) *x*,−1+*y*, *z*; c) *x*, 1+*y*, *z*; d)1+*x*, *y*, *z* for OCC **2**.

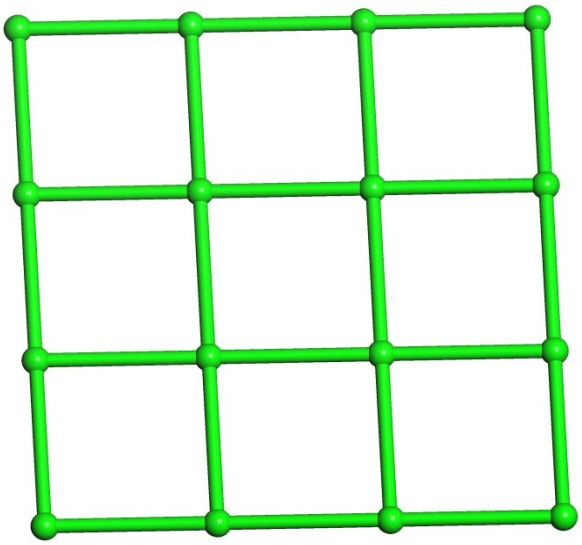

**Fig. S1** A 2D supramolecular network with (4, 4) topology in OCC **1**.

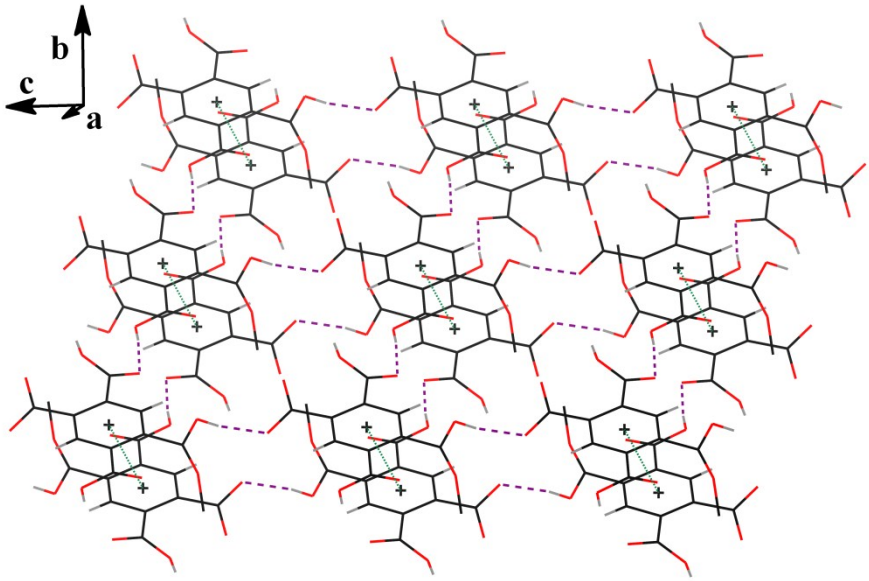


**Fig. S2** The π–π stacking interactions of benzene rings in two adjacent layers in OCC **1**.

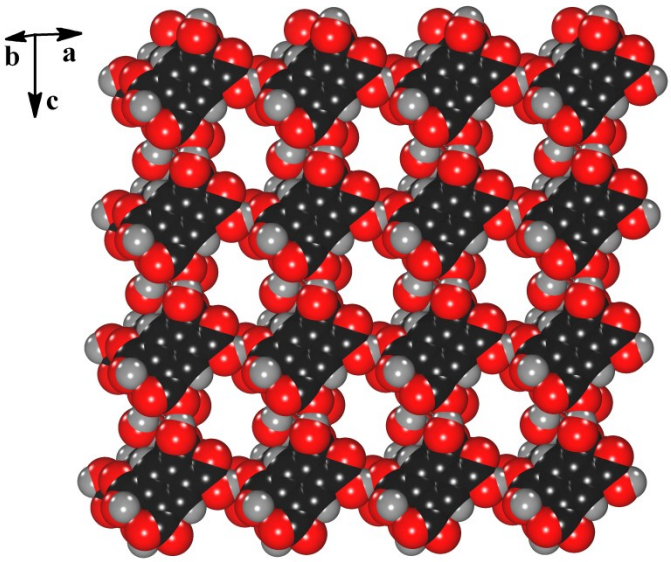


**Fig. S3** The cavity with dimensions of 5.497×8.062 Å$^2$ in OCC **1**.

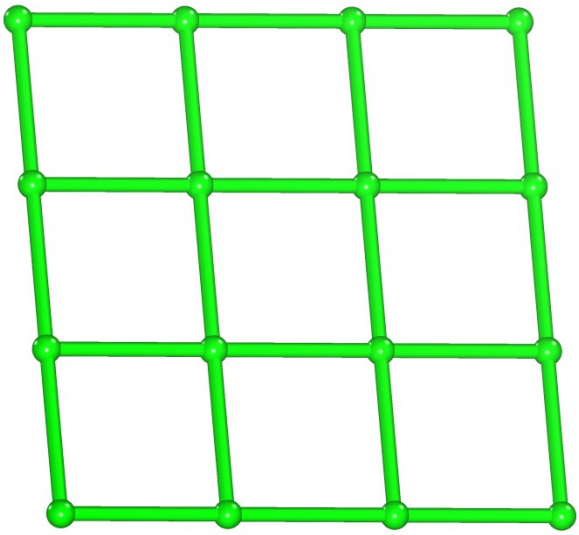

**Fig. S4** A 2D supramolecular network with (4, 4) topology in OCC **2**.

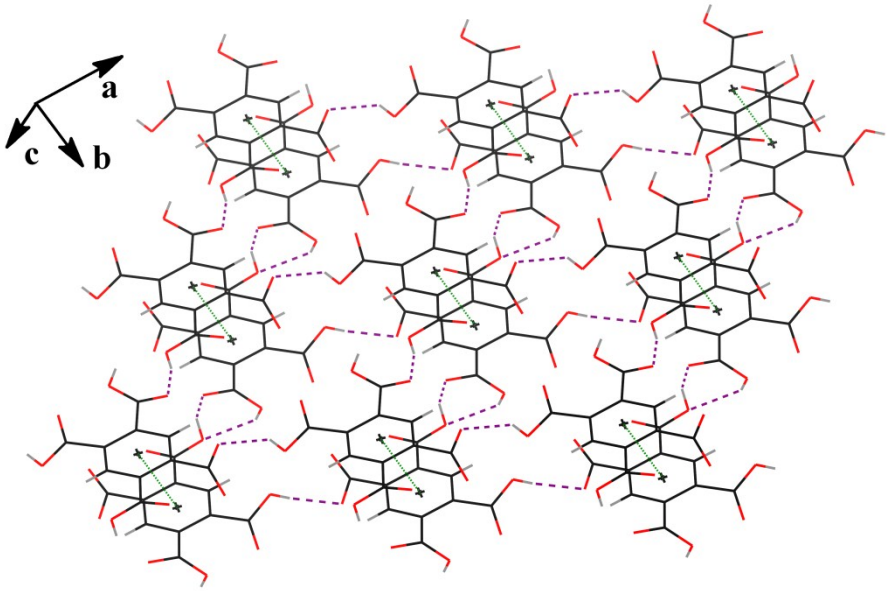


**Fig. S5** The π−π stacking interactions of benzene rings in two adjacent layers in OCC **2**.

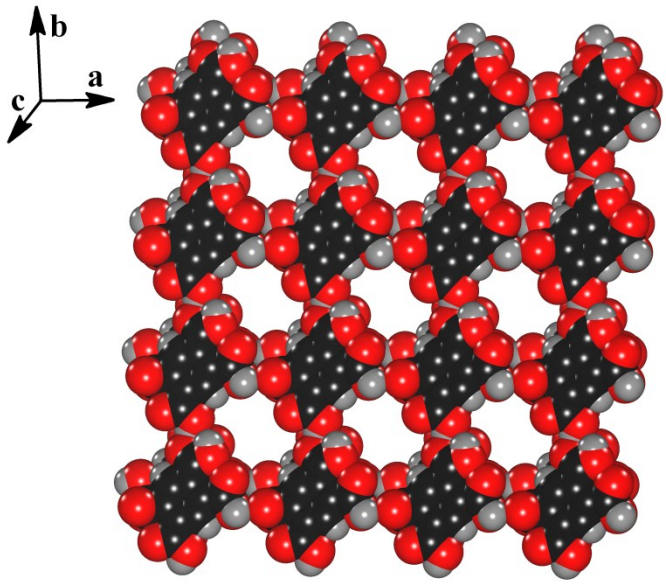


**Fig. S6** The cavity with dimensions of 5.486×8.040Å$^2$ in OCC **2**.

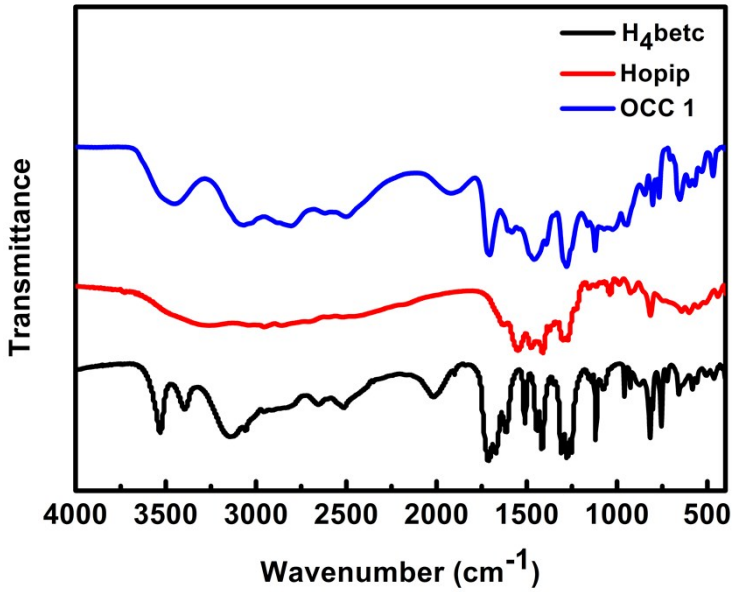


**Fig. S7** IR absorption spectra of $H_4$betc, Hopip and OCC **1** in the solid state at room temperature.

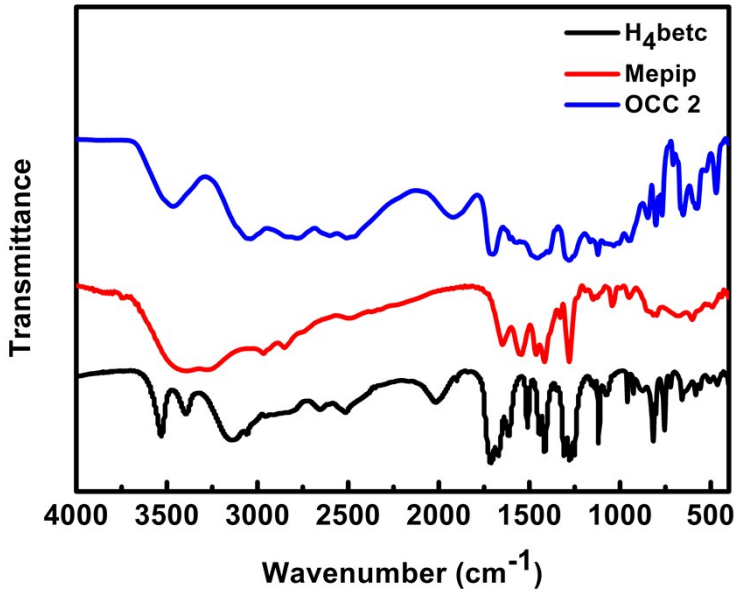


**Fig. S8** IR absorption spectra of $H_4$betc, Mepip and OCC **2** in the solid state at room temperature.

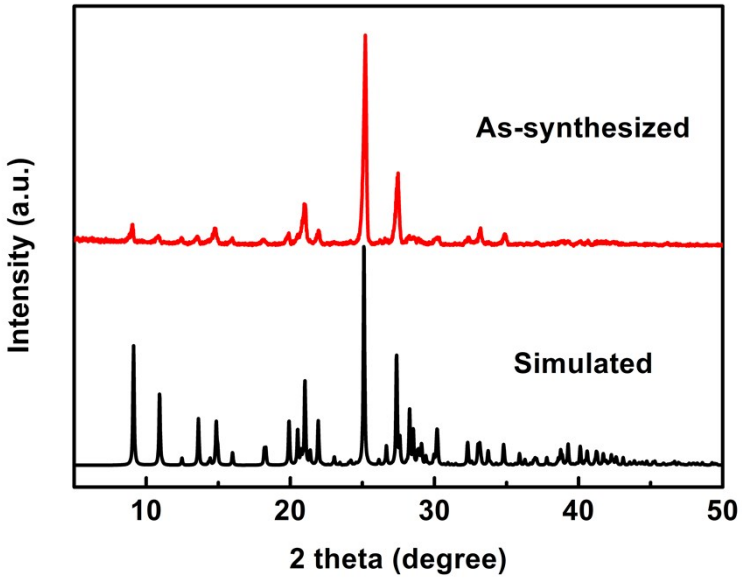


**Fig. S9** The PXRD patterns for OCC **1** of a simulation based on single-crystal analysis and as-synthesized bulk crystals.

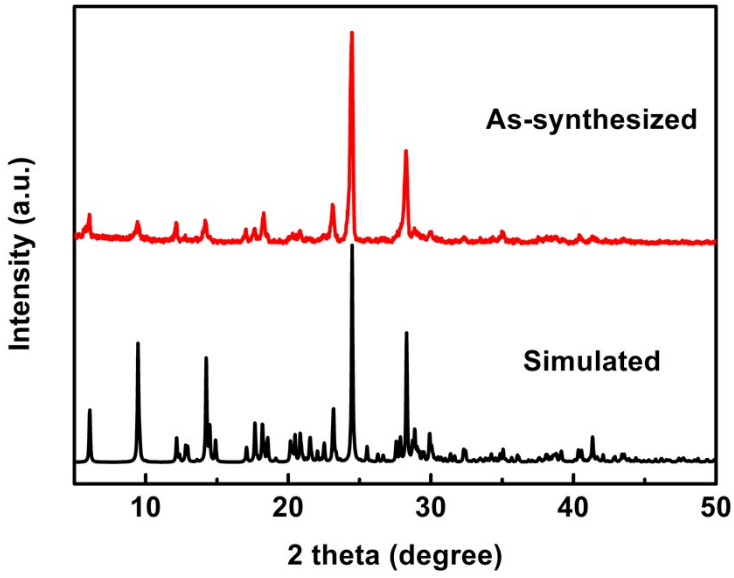


**Fig. S10** The PXRD patterns for OCC **2** of a simulation based on single-crystal analysis and as-synthesized bulk crystals.

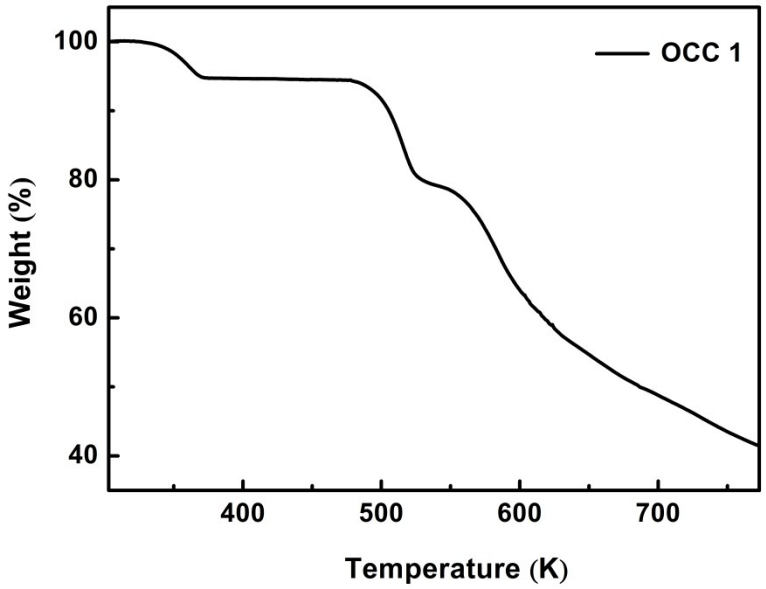


**Fig. S11** Thermogravimetric curve for OCC **1**.

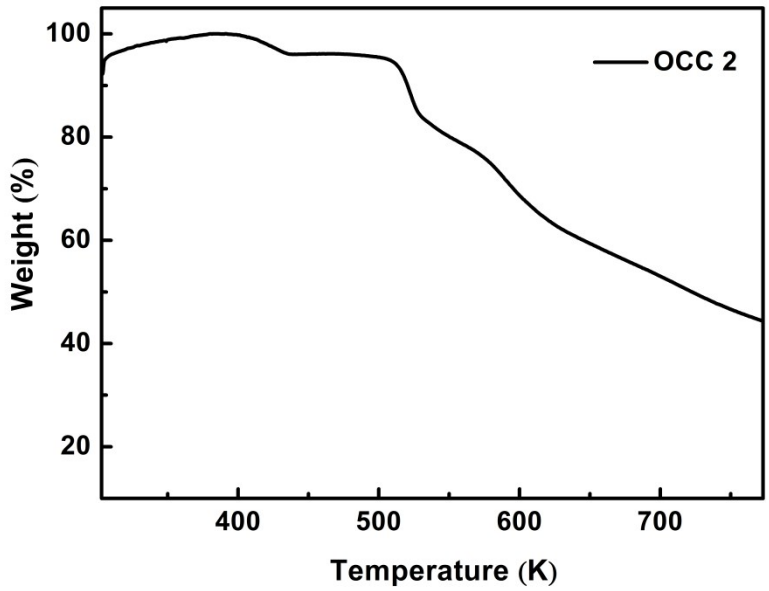


**Fig. S12** Thermogravimetric curve for OCC **2**.

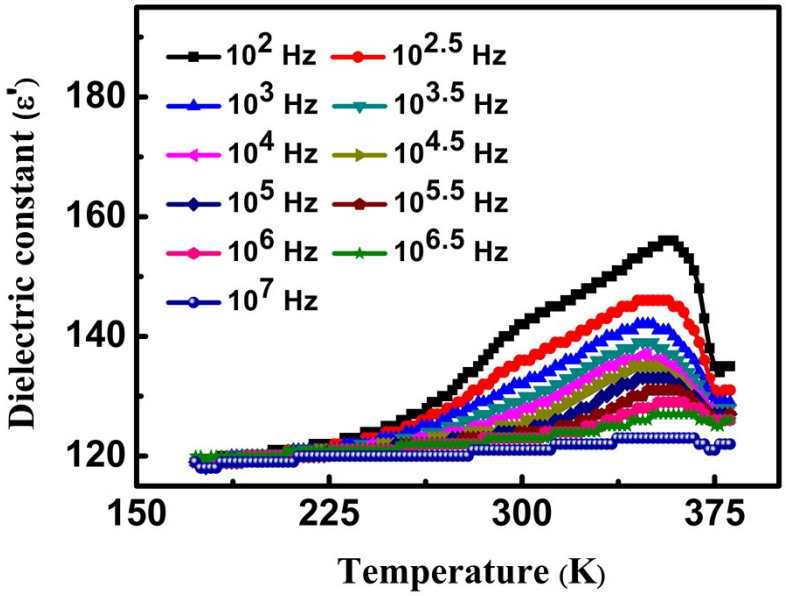


**Fig. S13** The dielectric constant (ε′) for OCC **1** measured as a function of temperature at various frequencies in the heating process.

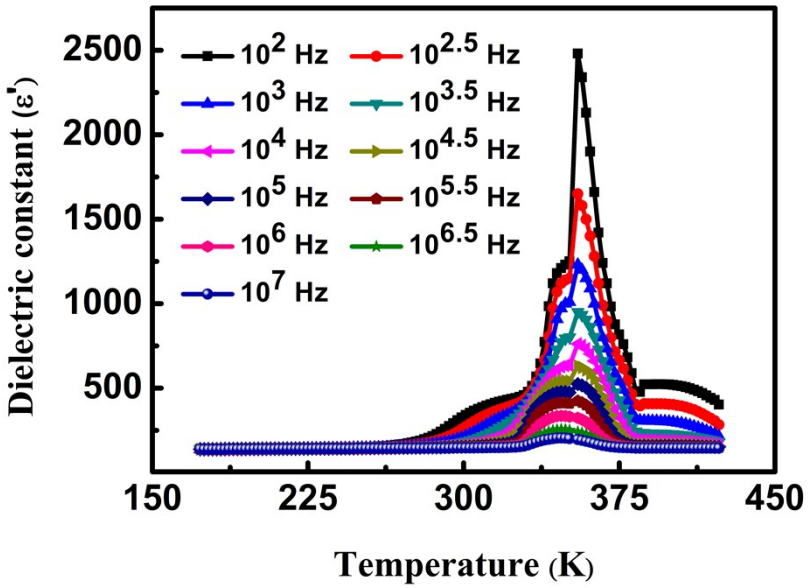


**Fig. S14** The dielectric constant (ε′) for OCC **2** measured as a function of temperature at various frequencies in the heating process.

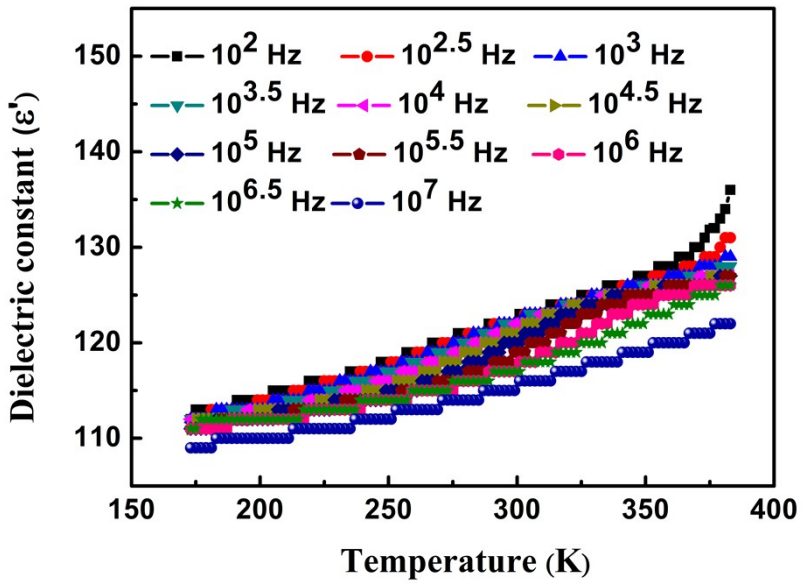


**Fig. S15** The dielectric constant (ε′) for OCC **1** measured as a function of temperature at various frequencies in the cooling process.

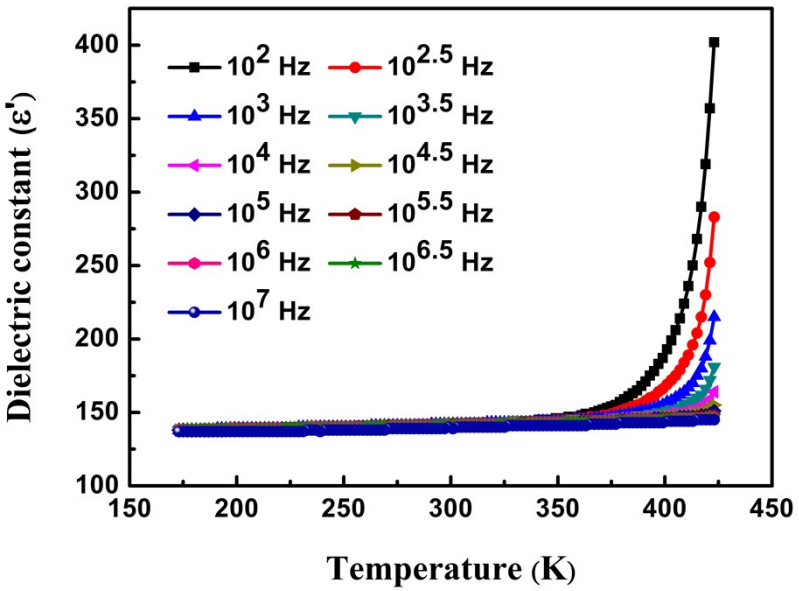


**Fig. S16** The dielectric constant (ε′) for OCC **2** measured as a function of temperature at various frequencies in the cooling process.

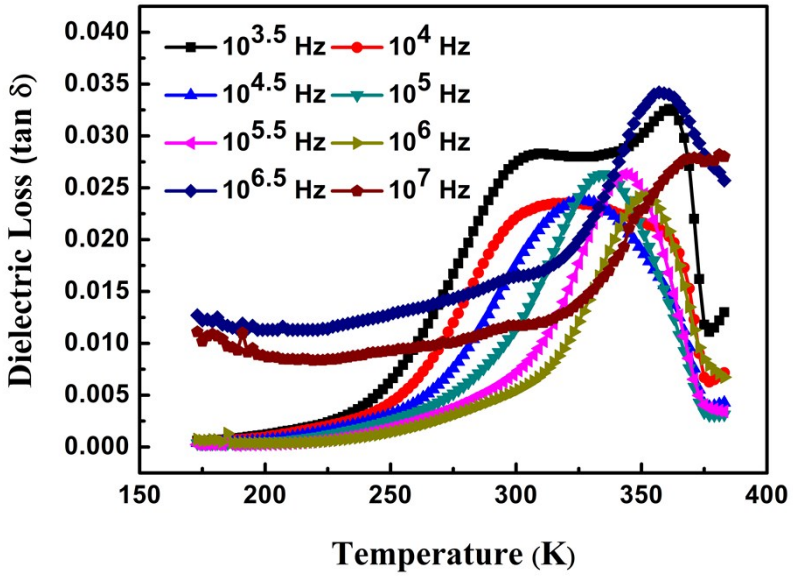


**Fig. S17** The dielectric loss (tan δ) for OCC **1** measured as a function of temperature at various frequencies in the heating process.

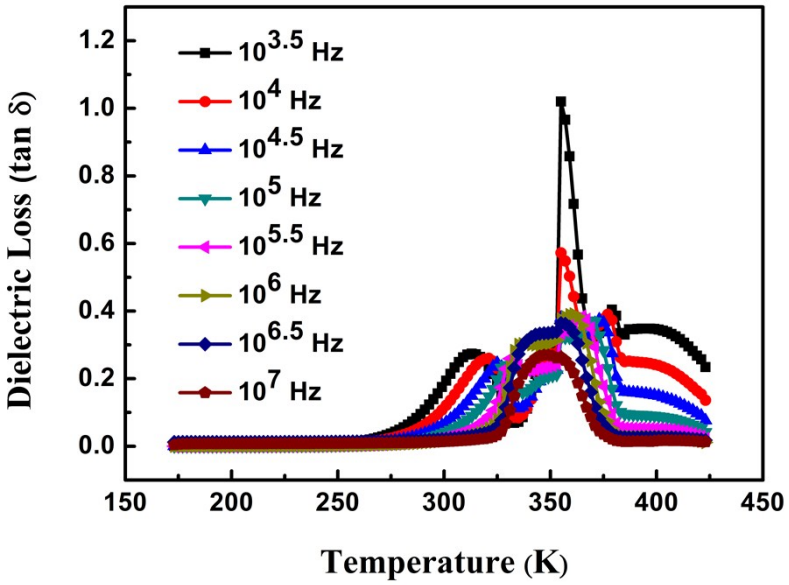


**Fig. S18** The dielectric loss (tan δ) for OCC **2** measured as a function of temperature at various frequencies in the heating process.

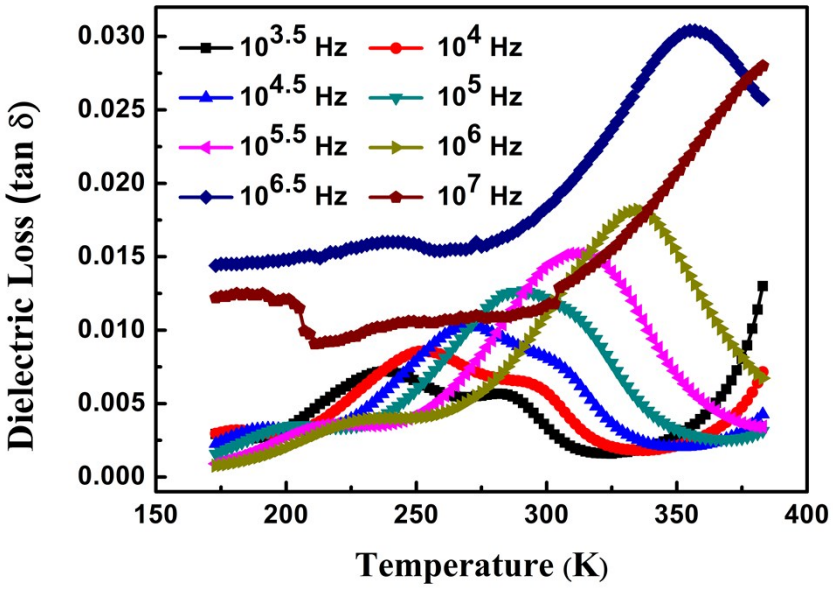


**Fig. S19** The dielectric loss (tan δ) for OCC **1** measured as a function of temperature at various frequencies in the cooling process.

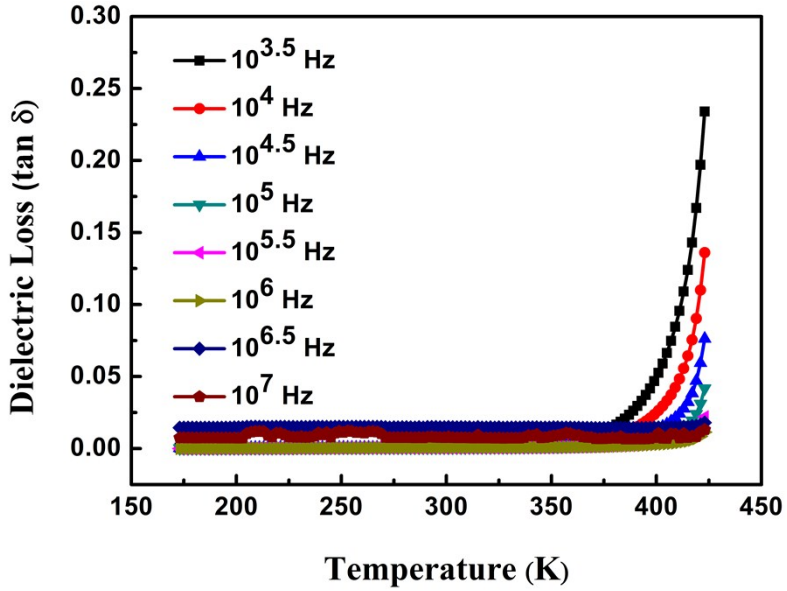


**Fig. S20** The dielectric loss (tan δ) for OCC **2** measured as a function of temperature at various frequencies in the cooling process.

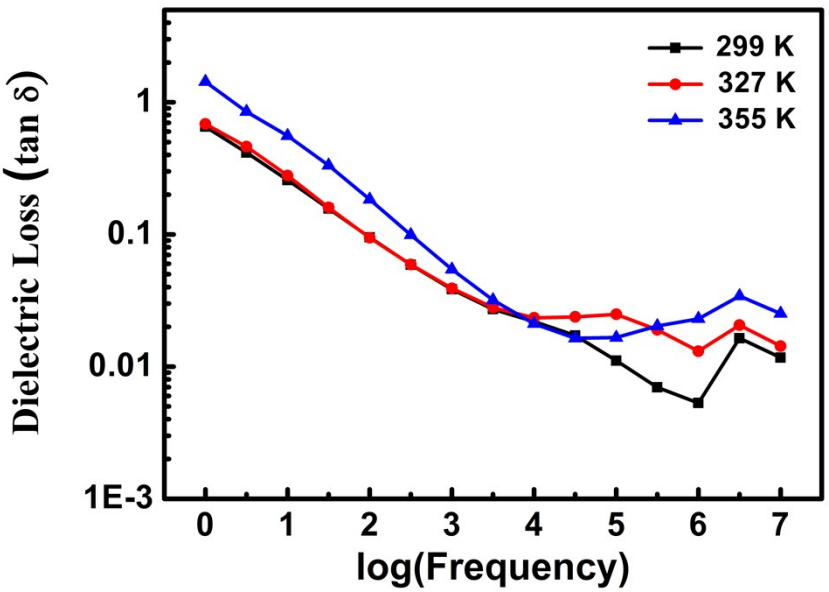


**Fig. S21** The dielectric loss (tan δ) for OCC **1** measured as a function of frequency at various temperatures in the heating process.

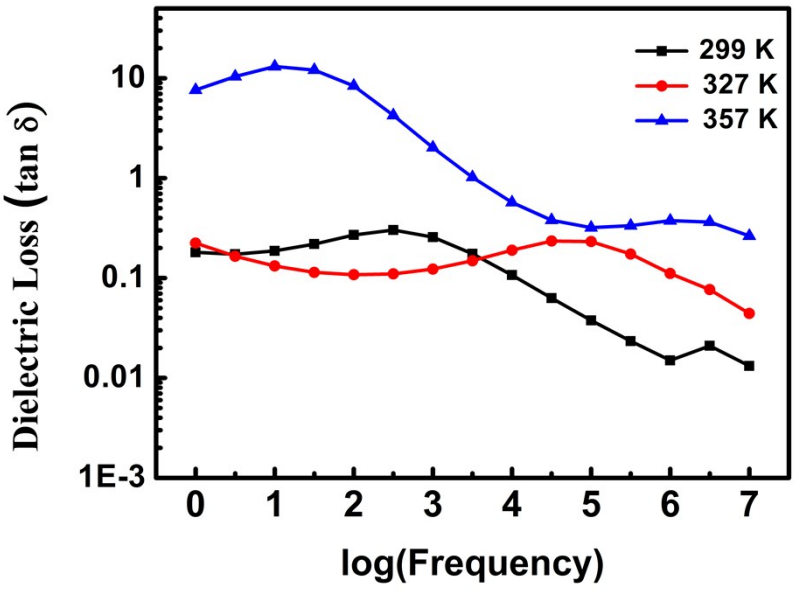


**Fig. S22** The dielectric loss (tan δ) for OCC **2** measured as a function of frequency at various temperatures in the heating process.

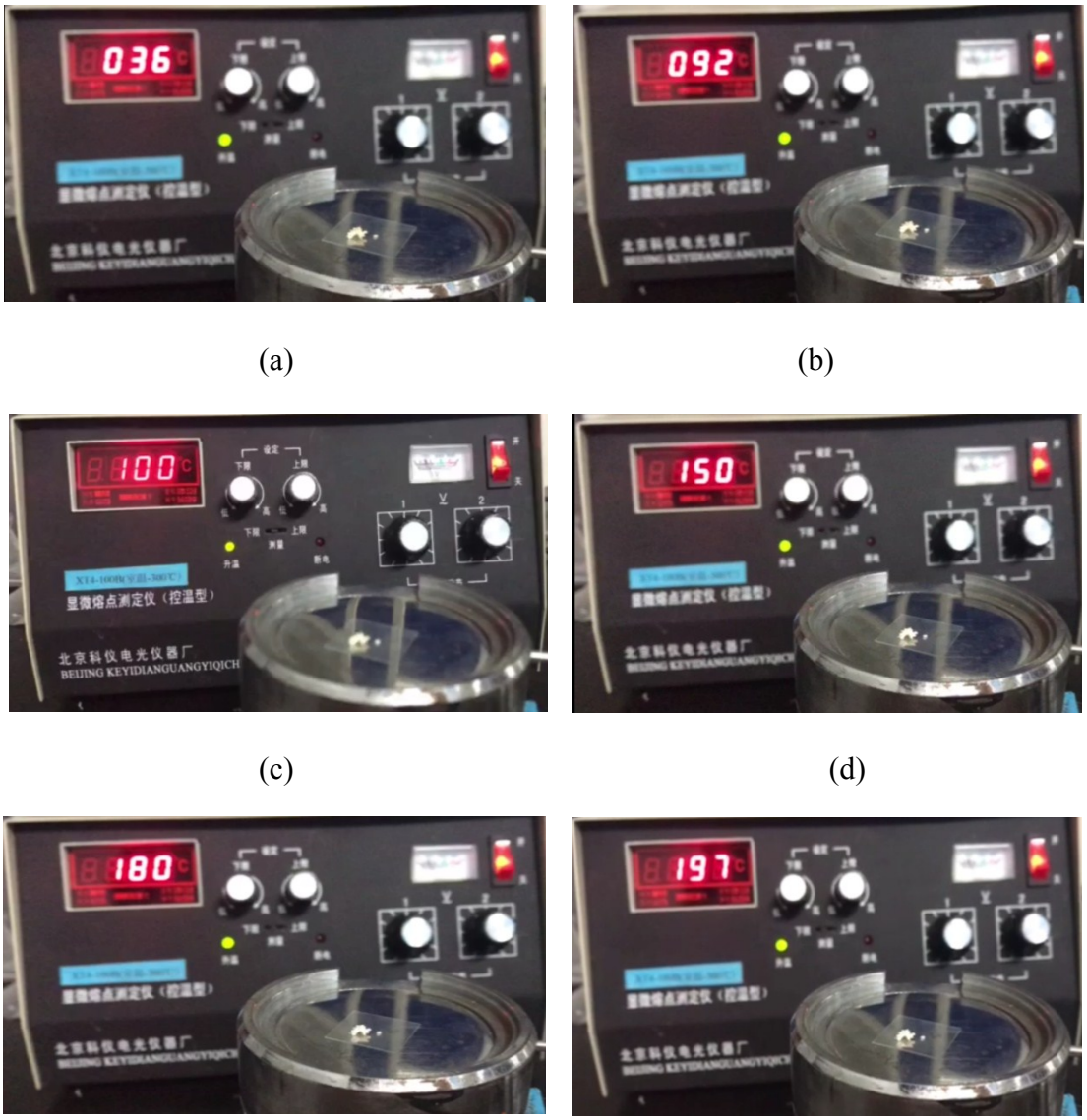


(a) (b)

(c) (d)

(e) (f)

**Fig. S23** Plots of the state of OCC **1** at (a) 36 ℃(309 K), (b) 92 ℃(365 K), (c) 100 ℃(373 K), (d) 150 ℃(423 K), (e) 180 ℃(453 K), (f) 197 ℃(470 K) in the process of melting point measurement.


(a)


(b)


(c)


(d)


(e)


(f)

**Fig. S24** Plots of the state of OCC **2** at (a) 36 ℃(309 K), (b) 111 ℃(384 K), (c) 122 ℃ (395 K), (d) 150 ℃(423 K), (e) 180 ℃(453 K), (f) 197 ℃(470 K) in the process of melting point measurement.

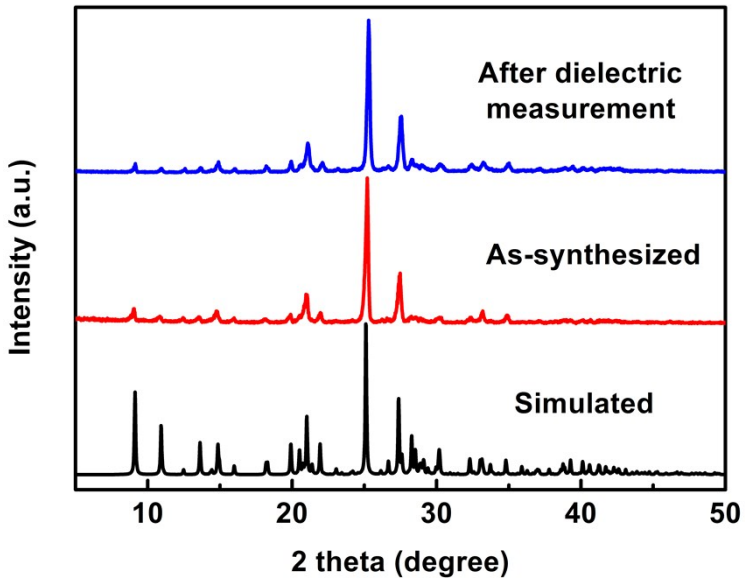


**Fig. S25** The PXRD patterns for OCC **1** of samples after the dielectric measurement, as-synthesized and simulated from single-crystal.

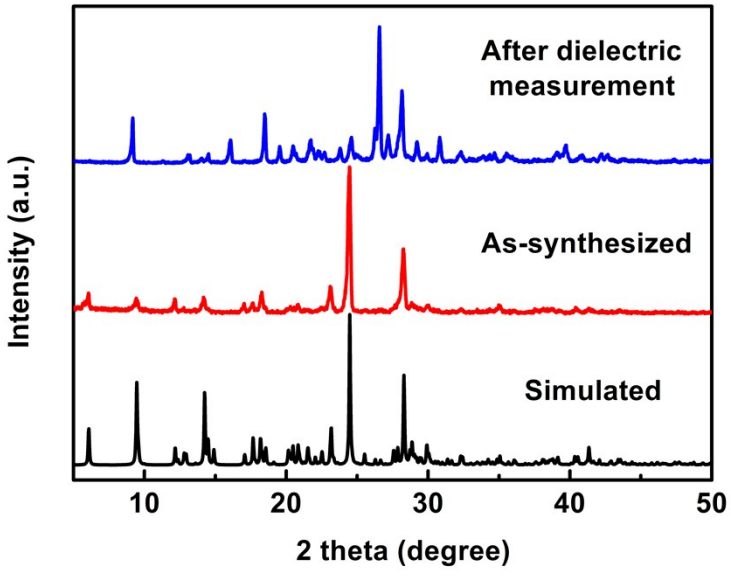


**Fig. S26** The PXRD patterns for OCC **2** of samples after the dielectric measurement, as-synthesized and simulated from single-crystal.

**Table S2.** Raman frequencies ($cm^{-1}$) of OCC **1** and OCC **2** and suggested assignment

| Raman frequency ($cm^{-1}$) | Suggested assignment |
|---|---|
| | OCC 1 |
| 676(m) | $\gamma(-NH^{2+})^a$ |
| 741(m), 773(m),782 (vw) | $\gamma(-NH^{2+})^b$ |
| 800(m), 808(s) | $\nu_{asym}(O-H\cdots O)$ |
| 1163(m) | $\beta(C-H)$ |
| 1259(m), 1390(s) | $\nu_{asym}(-COO^-)$ |
| 1567(w), 1608(s), 1565(w) | $\nu_{sym}(-COO^-)$ |
| 1703(w) | $\nu(C=O) + \delta(OH)$ |
| | OCC 2 |
| 675(m) | $\gamma(-NH^{2+})^a$ |
| 782(w), 792(w) | $\gamma(-NH^{2+})^b$ |
| 800(m), 808(s) | $\nu_{asym}(O-H\cdots O)$ |
| 1167(s) | $\beta(C-H)$ |
| 1261(vw), 1391(s) | $\nu_{asym}(-COO^-)$ |
| 1570(m), 1607(s) | $\nu_{sym}(-COO^-)$ |
| 1722(vw) | $\nu(C=O) + \delta(OH)$ |

[a]wagging mode; [b] twist mode; γ−deformation out of plane; $\nu_{asym}$ − asymmetric stretching; $\nu_{sym}$− symmetric stretching; β −in-plane-bending; δ − deformation in plane; vw−very weak, w−weak, m−medium, s−strong.

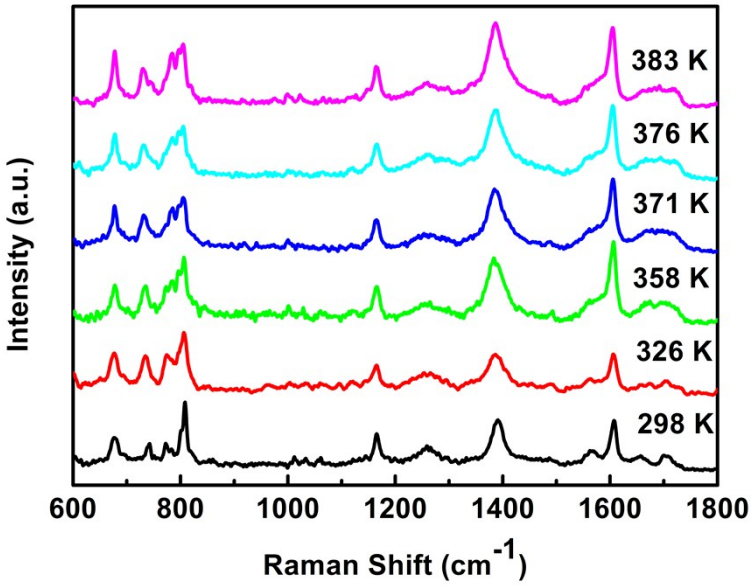


**Fig. S27** Temperature evolution of Raman bands of OCC **1** in the region of 600−1800 $cm^{-1}$.

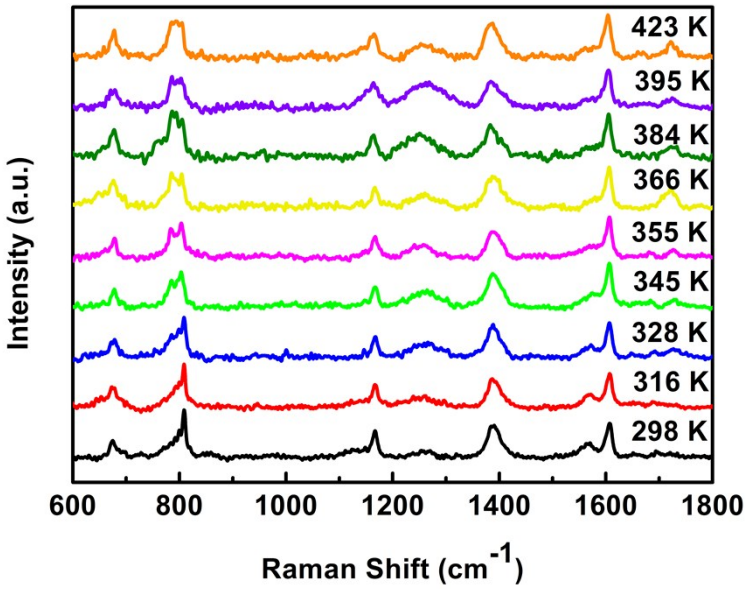


**Fig. S28** Temperature evolution of Raman bands of OCC **2** in the region of 600−1800 $cm^{-1}$.

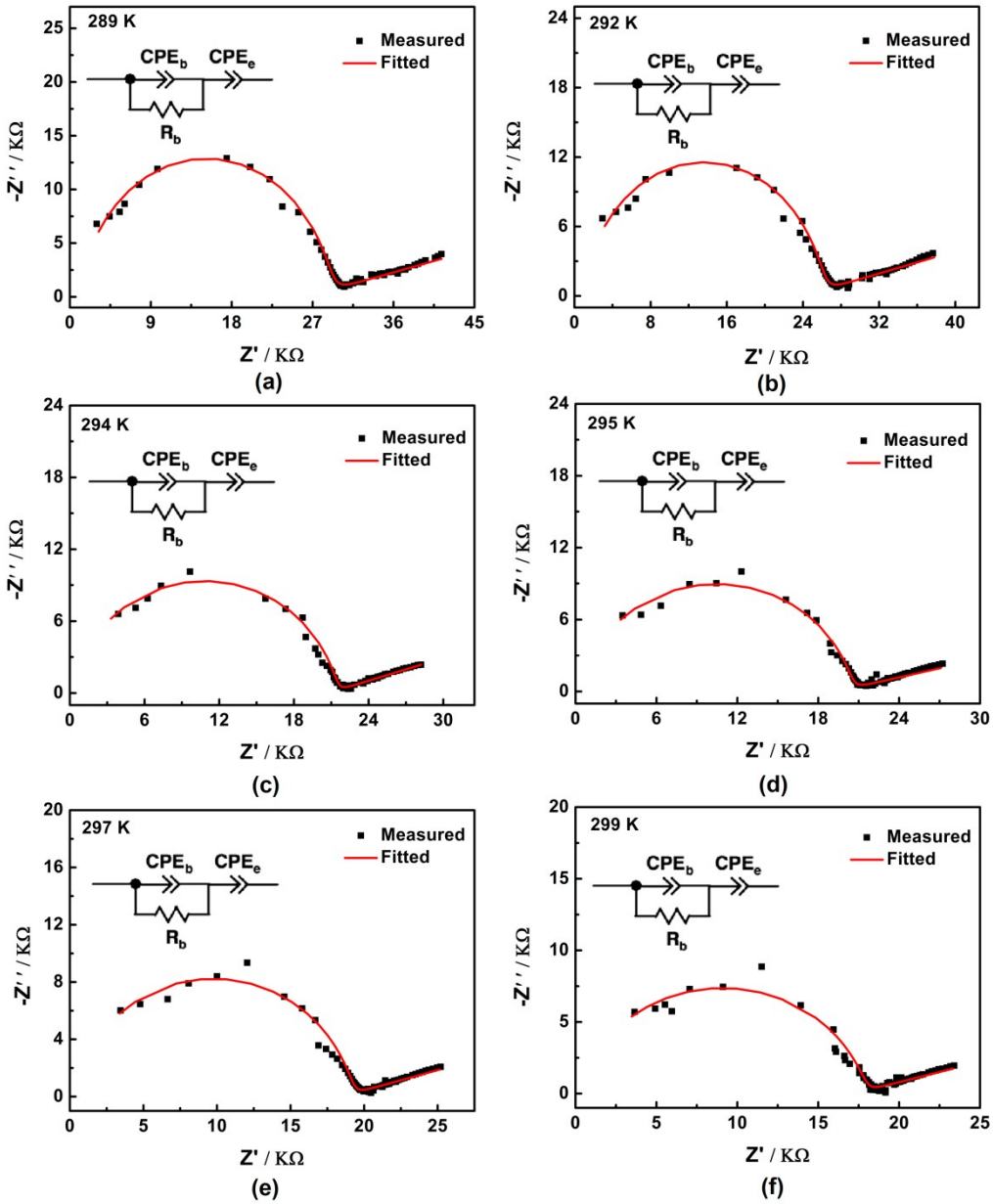


**Fig. S29** Nyquist plots of OCC **1** at different temperatures and ~97% RH (relative humidity).

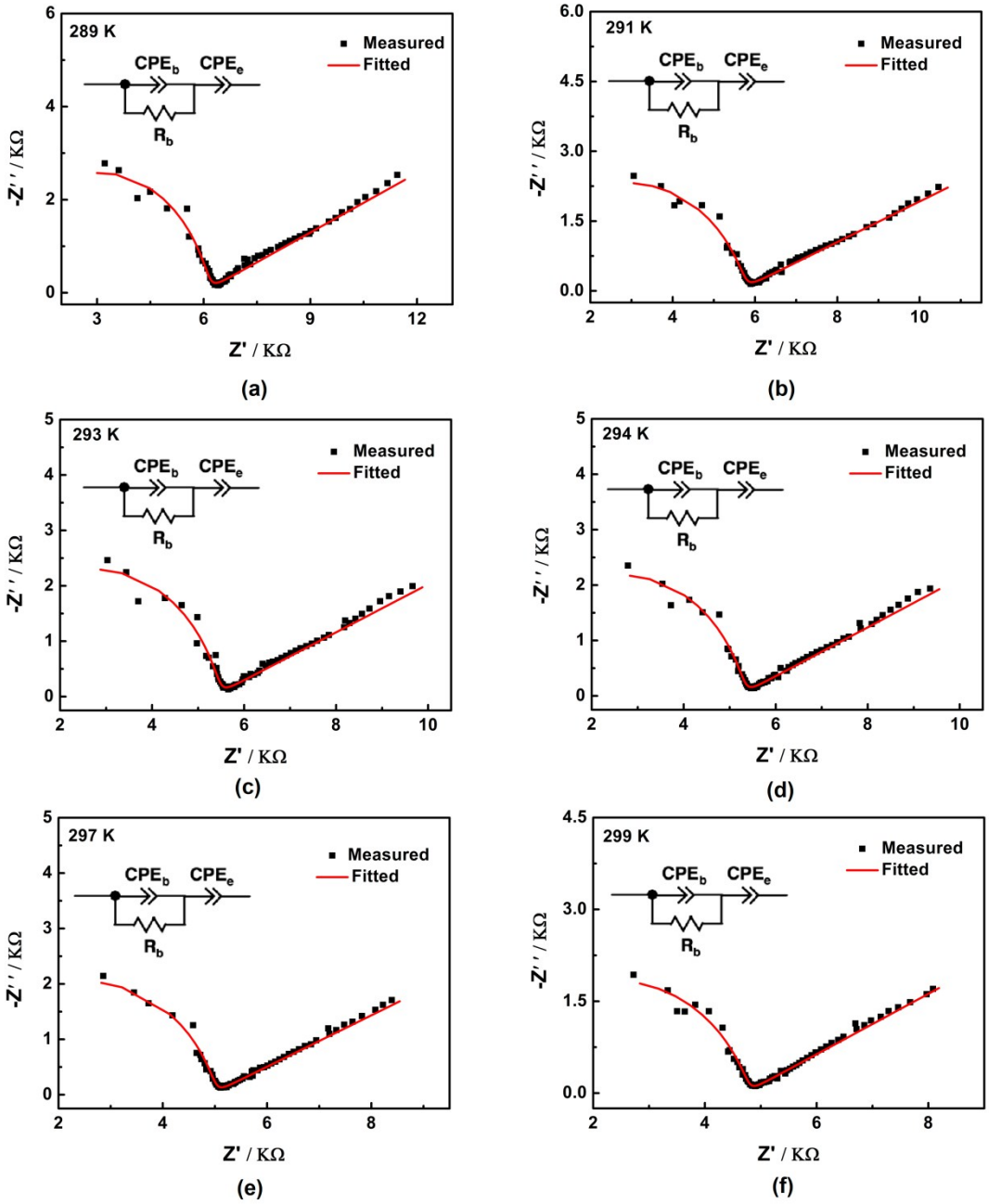


**Fig. S30** Nyquist plots of OCC **2** at different temperatures and ~97% RH (relative humidity).

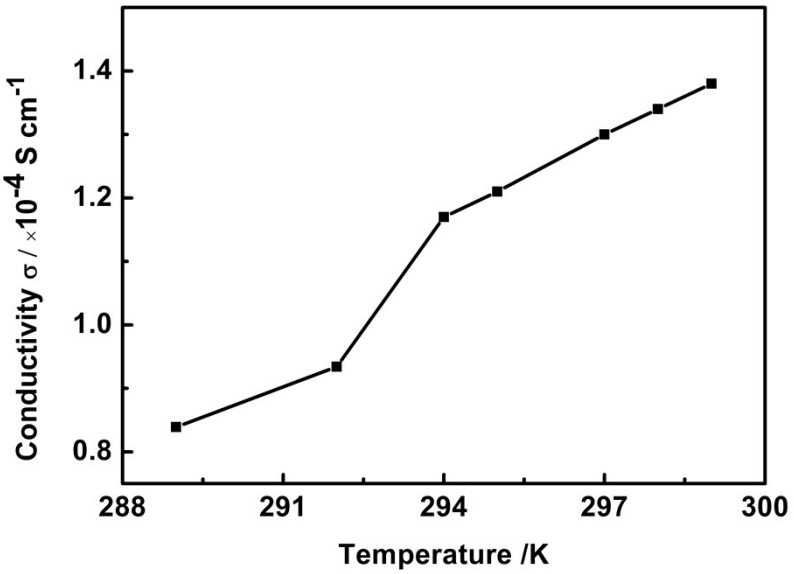


**Fig. S31** Temperature dependence of the conductivity (σ) for OCC **1** at ~97% RH.

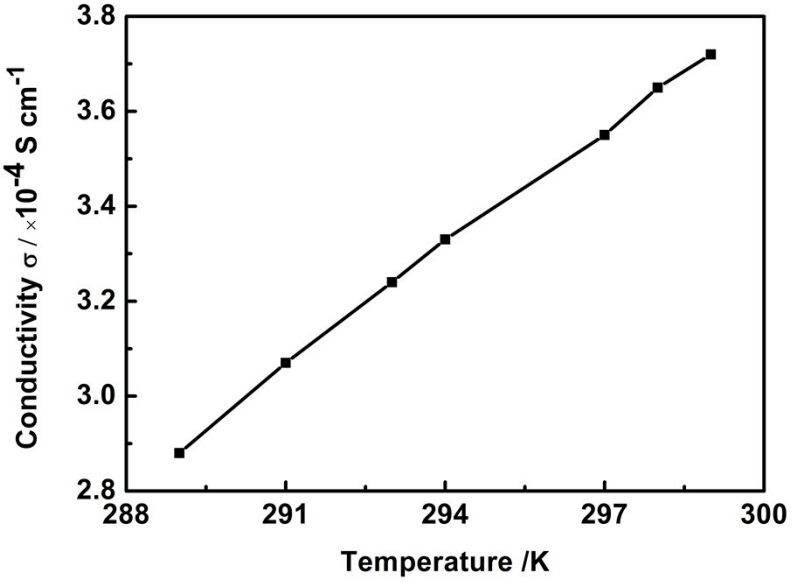


**Fig. S32** Temperature dependence of the conductivity (σ) for OCC **2** at ~97% RH.

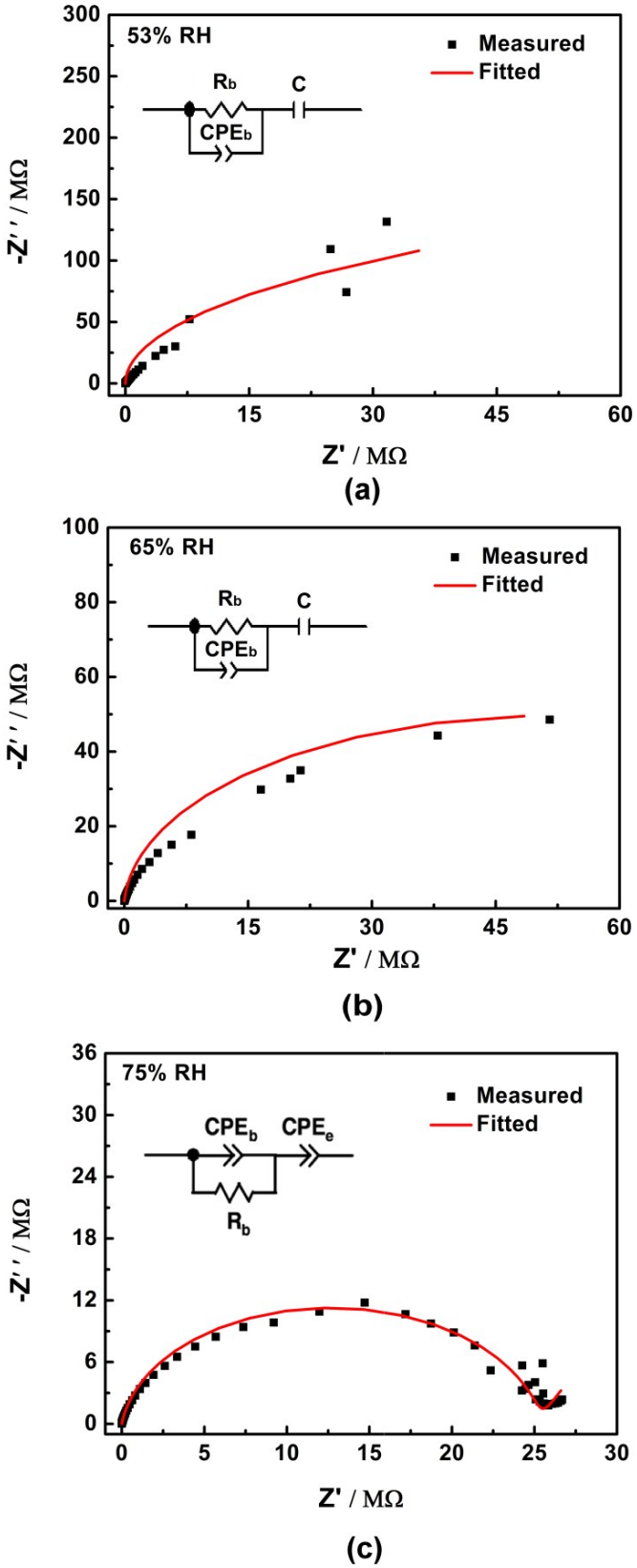


**Fig. S33** Nyquist plots of OCC **1** at different RH (relative humidity) and 298 K.

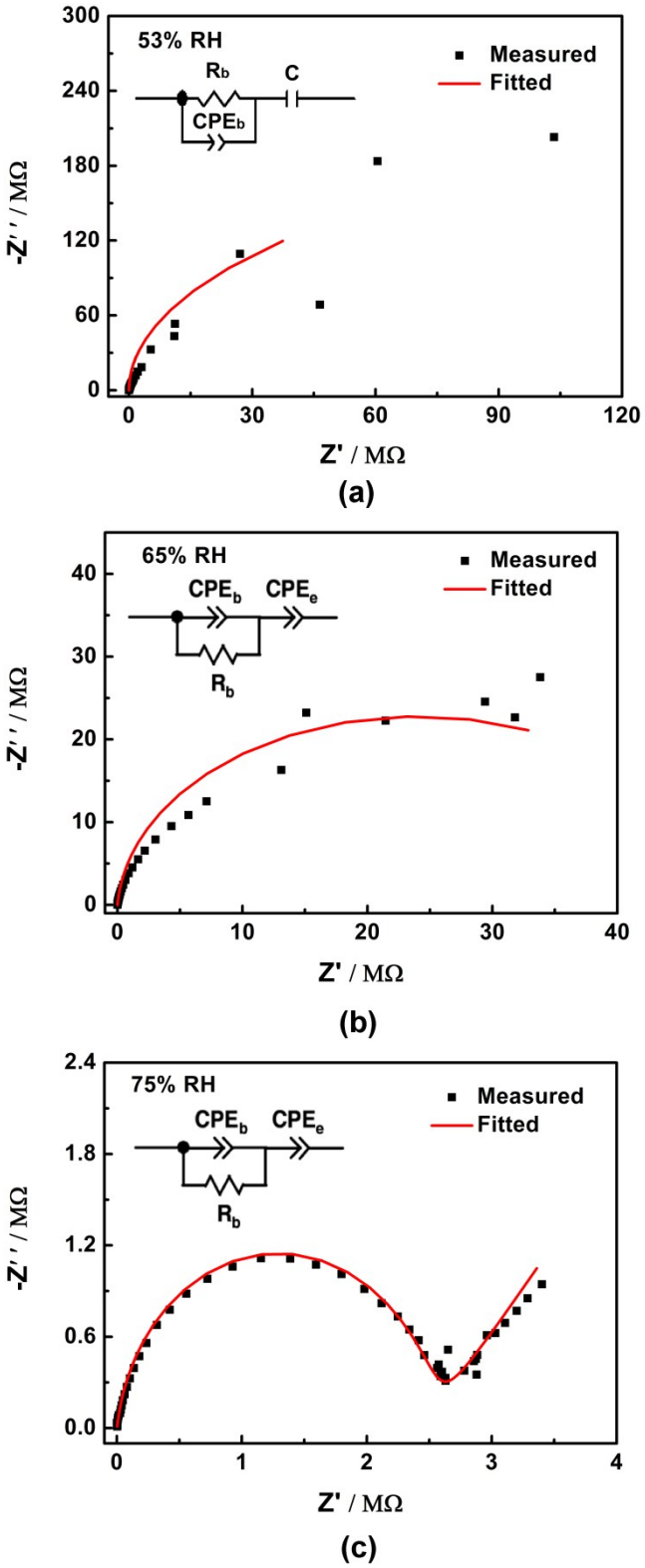


**Fig. S34** Nyquist plots of OCC **2** at different RH (relative humidity) and 298 K.

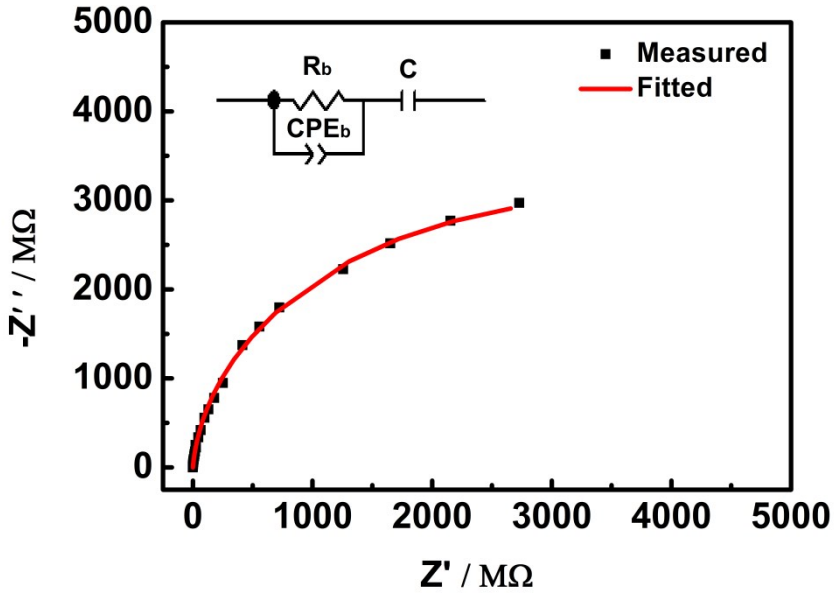


**Fig. S35** Nyquist plot of OCC **1** at ambient conditions and at 299 K.

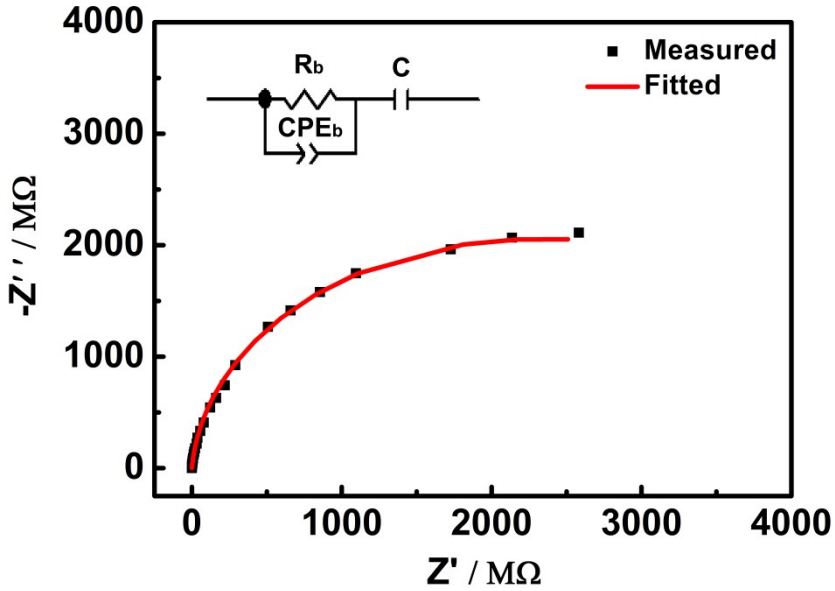


**Fig. S36** Nyquist plot of OCC **2** at ambient conditions and at 299 K.

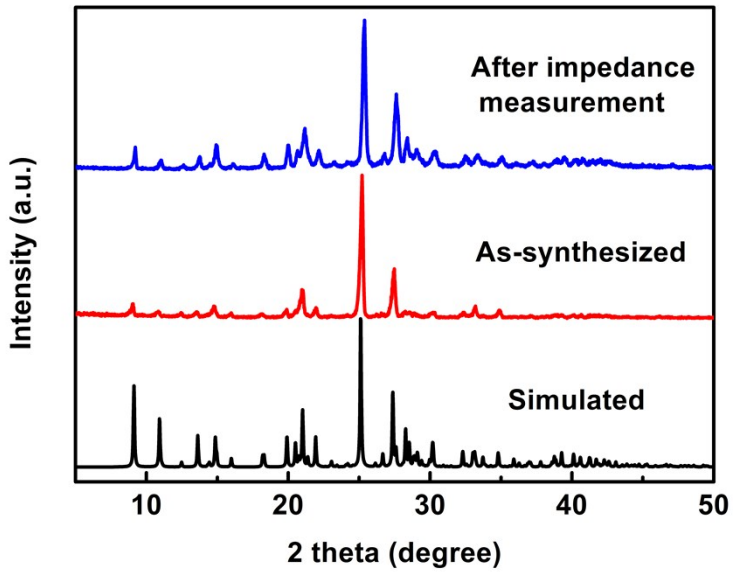


**Fig. S37** The PXRD patterns for OCC **1** of samples after the impendence measurement, as-synthesized and simulated from single-crystal.

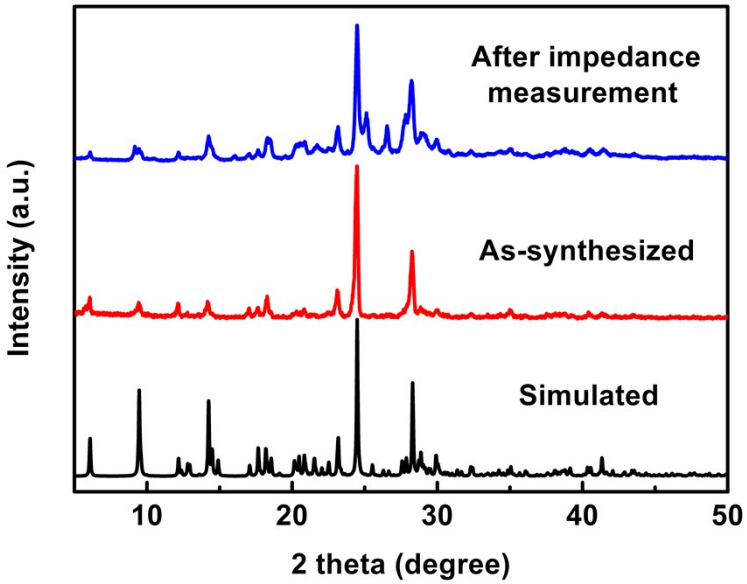


**Fig. S38** The PXRD patterns for OCC **2** of samples after the impendence measurement, as-synthesized and simulated from single-crystal.